Electronic Supplementary Material (ESI) for Energy & Environmental Science.

Electronic Supplementary Information

Quantification of the loss mechanisms in emerging water splitting photoanodes through empirical extraction of the spatial charge collection efficiency

Gideon Segev[1,2], Chang-Ming Jiang[1,2], Jason K. Cooper[1,2], Johanna Eichhorn[1,2], Francesca M. Toma[1,2], Ian D. Sharp[1,2,3,*]

[1]Chemical Sciences Division, Lawrence Berkeley National Lab, Berkeley, CA 94720, USA

[2]Joint Center for Artificial Photosynthesis, Lawrence Berkeley National Lab, Berkeley, CA 94720, USA

[3]Walter Schottky Institut and Physik Department, Technische Universität München, 85748 Garching, Germany

[*]sharp@wsi.tum.de

SEM image of as-deposited γ-$Cu_3V_2O_8$ photoanodes

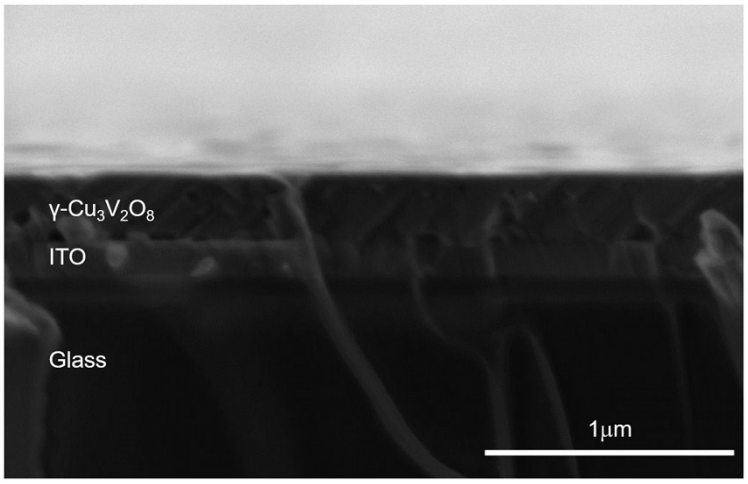

Figure S1: Cross sectional scanning electron microscope (SEM) image of a γ-$Cu_3V_2O_8$ photoanode deposited under the same conditions as those samples analyzed in this work.

Extraction of optical constants and optical generation profiles

The optical constants of the ITO and γ-$Cu_3V_2O_8$ layers where extracted by fitting variable angle spec-ellipsometry data to oscillators and shape-persevering functions (spline), respectively. In most cases it is more appropriate to use physical oscillator models for fitting spectroscopic ellipsometry data. However, lacking theoretical knowledge about the γ-$Cu_3V_2O_8$ optical properties, use of such models can result in overfitting the experimental data without producing more physical estimation of the optical constants. In order to test the extracted optical constants, those were used as inputs in a transfer matrix method (TMM) based optical simulator aiming to reproduce the transmission and reflection properties obtained by UV-Vis measurements. We have found that the best agreement was obtained by using a gradient γ-$Cu_3V_2O_8$ layer where the optical constants change linearly with the distance from the surface. The gradient in the refractive index may be a result of small variations in composition which may also account for the frequency dependent Mott Schottky plots shown in Figure S11. Figure S2 shows the extracted optical constants for ITO and γ-$Cu_3V_2O_8$; more information about the fitting process can be found in the methods section. Figure S3 shows the calculated optical

generation profiles for various wavelengths under front and back illumination, as calculated with the TMM using the optical constants shown in Figure S2.

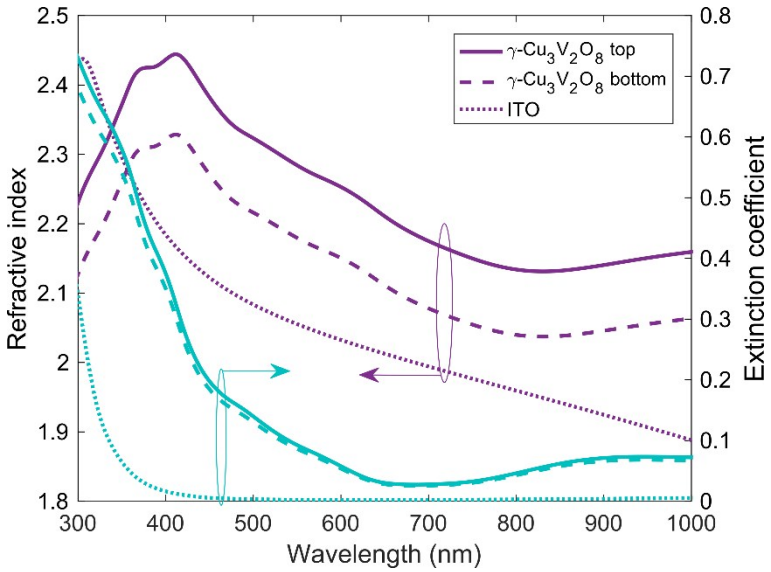

Figure S2: ITO and γ-$Cu_3V_2O_8$ optical constants obtained from variable angle spectroscopic ellipsometry.

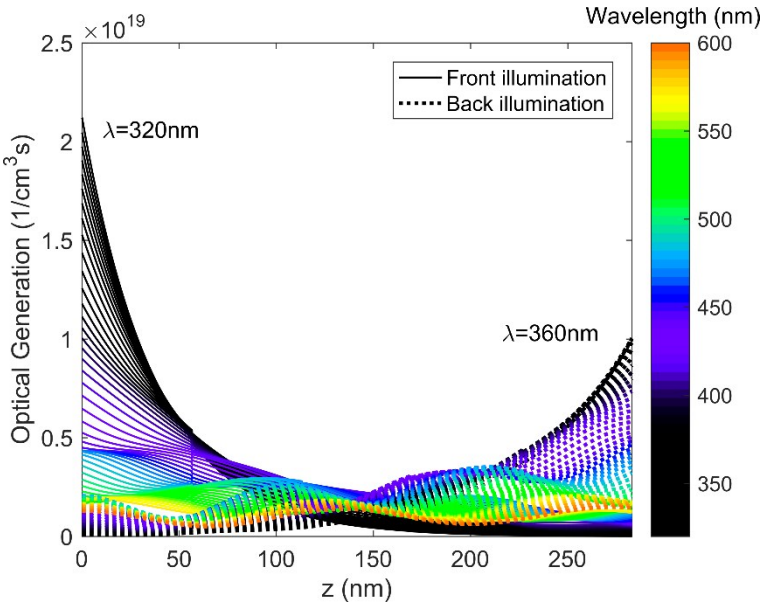

Figure S3: The optical generation profiles, as calculated with the TMM for various incident wavelengths, under front and back illumination. The optical constants used in the calculation are those given in Figure S2. This plot was generated using an incident photon flux of 10^{14} photons/cm^2s for all incident wavelengths.

Stability and repeatability of IPCE measurements

Previously, we found γ-$Cu_3V_2O_8$ to be stable for at least 20 h of sustained operation in 0.1 M sodium borate buffer solution at pH 9.3, as determined by chronoamperometry.[1] In the present work, we further verify the stability and

measurement repeatability by conducting a series of IPCE measurements over the course of 5 h, during which the potential was switched back and forth between 1.25 V vs. RHE and 1.85 V vs. RHE. Four sets of IPCE scans were conducted at 1.25 V vs. RHE and three sets were conducted at 1.85 V vs. RHE, where each set comprised seven IPCE spectra (giving a total of 49 spectra altogether). The measurement time for the seven spectra at 1.85 V vs. RHE was about 30 minutes and at 1.25 V vs. RHE was about 50 minutes, yielding a total measurement time of nearly 5 hours. Figure S4 shows the IPCE spectra measured in this series. The markers indicate the mean value of the seven IPCE spectra in every set and the error bars, which are on the order of the size of the markers, indicate the standard deviation between the measurements. The legend notes the order in which the sets were taken. Despite the potential being ramped back and forth for an extended period of time, the measured IPCE spectra show no statistically significant changes.

Morphological stability during the 5 h measurement sequence was also confirmed by AFM, as shown in Figure S5. The RMS roughness values before and after the IPCE measurement were 12.3 nm and 13.3 nm, respectively. The very small change in the IPCE spectra shown in Figure S4 and the small changes in topography, as shown in Figure S5, demonstrate the excellent stability of the photoanodes during the measurements.

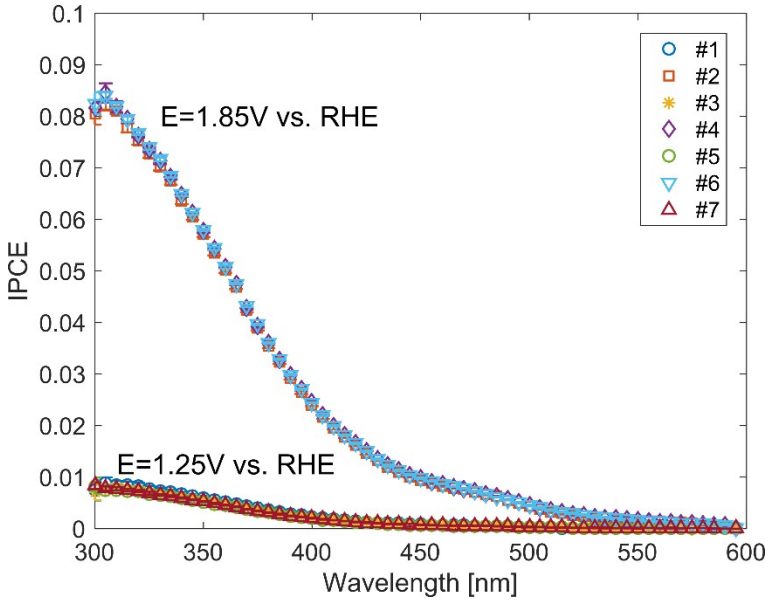

Figure S4: IPCE measurements taken for the stability analysis. Each marker is the mean value of a set of seven consecutive measurements and the error bars indicate the standard deviation of the measurement within each set. The legend indicates the order in which the sets of measurements were conducted.

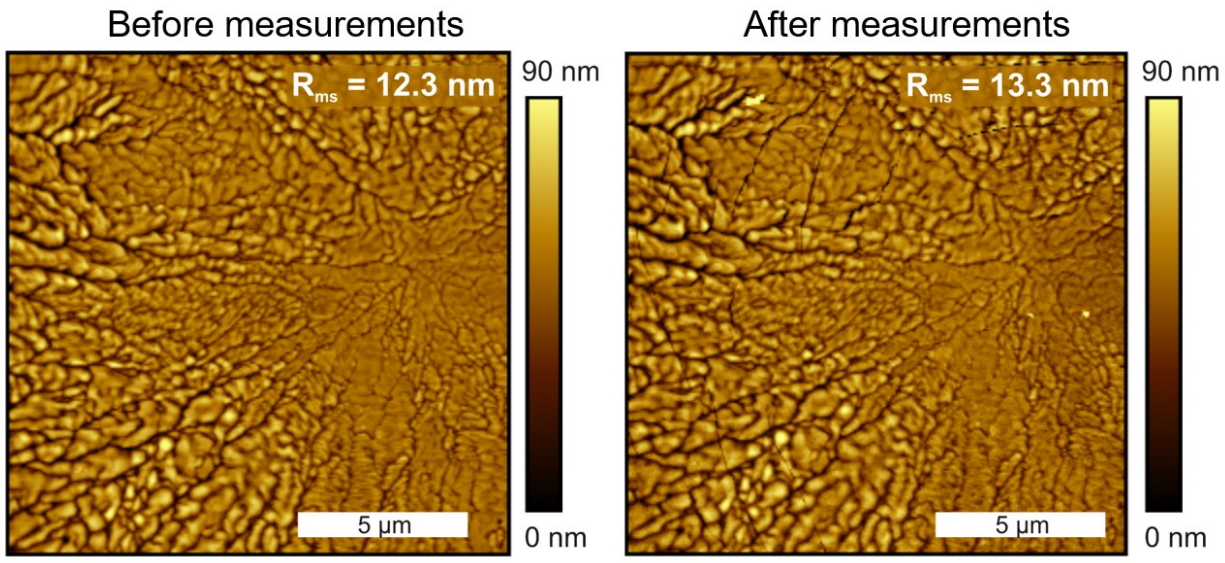

Figure S5: AFM topography maps taken before and after the IPCE measurements presented in Figure S4. The RMS roughness values before and after the IPCE measurement are 12.3 nm and 13.3 nm, respectively.

The regularization problem

The goal of the regularization process is to find a vector, $\phi(z_i)$, that minimizes the norm:

$$\epsilon = \left\| q \cdot \Delta\bar{G}'(\lambda,z_i)\phi(z_i) - \Delta J_{photo}(\lambda_i) \right\|_2 \quad \text{(S1)}$$

Since this is an ill-posed problem, there are an infinite number of possible solutions, of which only one is the physical solution. Thus, there is a need to constrain the solutions according to prior expectations of the values of $\phi(z_i)$. For example, in the systems tested here, $\phi(z_i)$ should not be higher than 1 (or lower than -1, depending on electrical current sign conventions), and it should not have an oscillating shape. One common method to impose such constraints is to add to equation (S1) a term describing the quantity to be constrained[2,3]:

$$\epsilon' = \left\| q \cdot \Delta\bar{G}'(\lambda,z_i)\phi(z_i) - \Delta J_{photo}(\lambda_i) \right\|_2 + \kappa \left\| L_n \phi(z_i) \right\|_2 \quad \text{(S2)}$$

Where L_n is the identity matrix for n=0 and the nth order derivative operator for n>0. κ is the regularization parameter, which defines the relative contribution of each of the two norms to the overall error. It should be stressed that constraining the second term in equation (S2) limits the ability to minimize the first term in this equation. For example, if L_n is the identity matrix, high values of κ will constrain the solution to have a small magnitude (or small gradients if $n = 1$ and small curvature for $n = 2$) but will not minimize ε. On the other hand, small values of κ lead to small values of the norm, ε, but provide few constraints on the solution. Hence, there is a tradeoff between over-constraining $\left\| L_n \phi(z_i) \right\|_2$, which may result in high values of ε, and under-constraining $\left\| L_n \phi(z_i) \right\|_2$, which results in unphysical solutions. This trade off can be solved by plotting $\left\| L \phi(z_i) \right\|_2$ against ε for different values of κ. Such a graph is usually characterized by an L-shape, where the knee of the curve corresponds to the regularization parameter, κ_{knee}, which minimizes both terms in equation (S2).[2,3] Figure S6 (a,b) show the *L* curves produced during the regularization process for the data presented in Figure 2 and 3, respectively. Since the solution fluctuates somewhat as the regularization parameter changes, solutions corresponding to regularization parameters in the range of $0.1\kappa_{knee} \leq \kappa \leq 10\kappa_{knee}$ were averaged to produce the final $\phi(z_i)$ profiles presented in Figures 2 and 3.

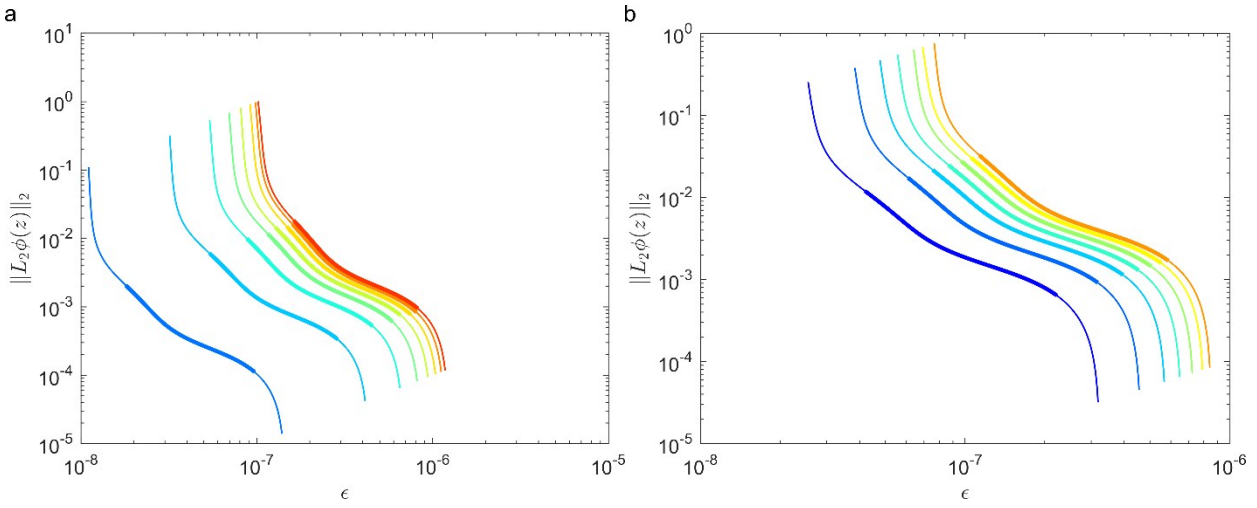

Figure S6: (a) L-curves produced in the regularization process for extracting $\phi(z_i)$ for the measurements shown in Figure 2. (b) L-curves produced in the regularization process for extracting $\phi(z_i)$ for the measurements shown in Figure 3. The thick lines represent points in which κ is in the range $0.1\kappa_{knee} \leq \kappa \leq 10\kappa_{knee}$. Solutions corresponding to regularization parameters in this range were averaged to obtain the final $\phi(z_i)$ profiles. The color coding is as in Figures 2 and 3.

The three main numerical handles that can be modified to extract the physical solutions are the regularization parameter, κ, the choice of operator, L_n, and the grid discretization. As already discussed, the regularization parameter can be chosen using an L-curve and identifying its knee. Other algorithms for identifying the optimal κ can be found in reference 3. In this work we have chosen L_n to be the second derivative operator, which produces smooth solutions. For this choice of operator, overconstraining the solution results in rounding of corners in the $\phi(z)$ profiles. Choosing L to be the identity matrix, i.e. constraining the norm of $\phi(z)$, resulted in very noisy solutions. The spatial grid used for the regularization process should be chosen according to prior knowledge of the system. Since in this work we chose to constrain the second derivative, the grid was chosen to be denser near the surface, where large gradients are expected, and sparser farther away from the surface. This allows the regularization process to remove unwanted curvatures from the solution without having to reduce the gradients near the surface. Figure S7 shows the spatial grid used in the $\phi(z)$ extraction process. Element number 1 is the element closest to the semiconductor/electrolyte interface and element number 99 is the farthest away from it.

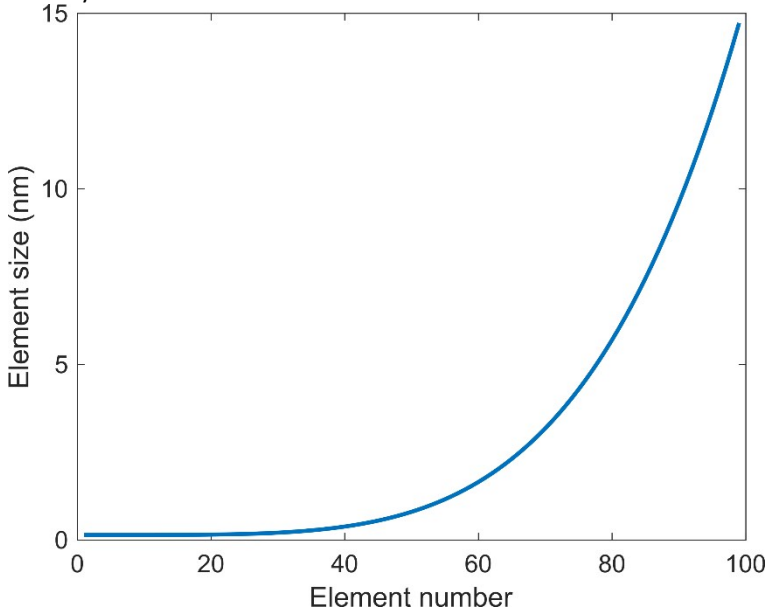

Figure S7: the spatial grid used in the $\phi(z)$ extraction process. Element number 1 is closest to the semiconductor/electrolyte interface and element number 99 is the farthest away from it.

Over-constrained solutions can be identified by trying to reconstruct the IPCE measurements with the optical generation matrix $\Delta\bar{G}(\lambda,z_i)$ and the extracted $\phi(z_i)$ profile, as described by equation (2).[4] As discussed above, reconstructed IPCE spectra produced from underconstrained solutions will reproduce the measured IPCE curves perfectly but ones produced from overconstrained solutions will deviate from it significantly. It should be noted that since some errors in the optical modeling are expected, even a perfect physical solution for $\phi(z)$ will not be able to reproduce the measured IPCE spectra and that the optical modeling errors will be translated directly to the reconstructed IPCE. For example, in case the modeled absorption is higher than the measured absorption, the reconstructed IPCE curve will be higher than the measured IPCE curve in the same wavelength range.

Figure S8 (a) shows the $\phi(z)$ curves produced by the IPCE curve shown in Figure 2(a) by averaging solutions over three different ranges of κ: $\kappa_{knee} \leq \kappa \leq 100\kappa_{knee}$ representing an over-constrained solution, $0.1\kappa_{knee} \leq \kappa \leq 10\kappa_{knee}$ representing a constrained solution with values near the knee of the curve, and $0.01\kappa_{knee} \leq \kappa \leq \kappa_{knee}$ representing an under-constrained solution. The potential at which the IPCE curve was measured is 1.5 V vs. RHE. Figure S8 (b) shows the measured IPCE and the IPCE curves calculated by inserting the $\phi(z)$ profiles from Figure S8 (a) into equation (2). As discussed above, the underconstrained solution shows a slightly oscillatory behavior and reaches values above 1 at the surface, deeming it unphysical. On the other hand, overconstraining the solution produces a $\phi(z)$ profile that might possess a physically reasonable shape. However, as shown in Figure S8 (b), the reconstructed IPCE curve produced by this profile deviates significantly from the measured IPCE spectrum.

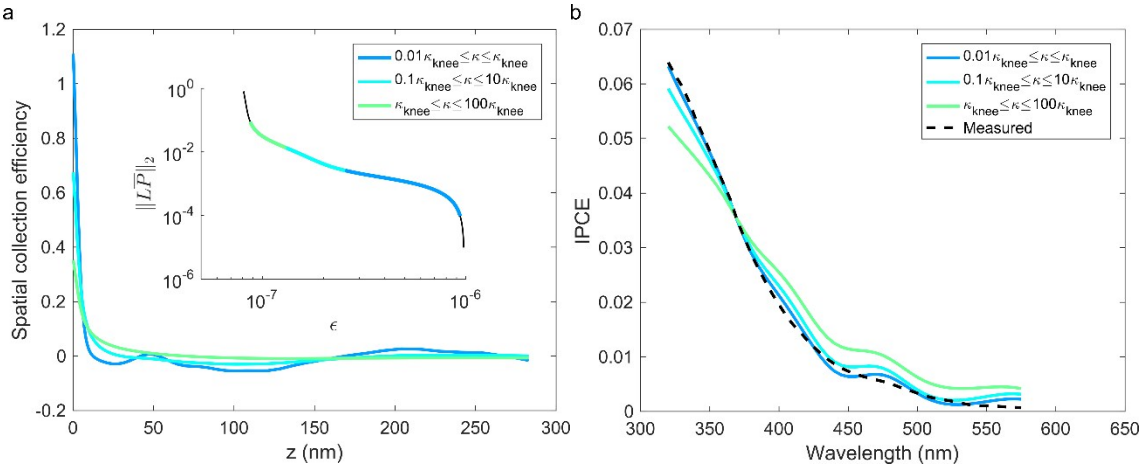

Figure S8: (a) The averaged $\phi(z)$ profiles using different ranges of regularization parameters: $\kappa_{knee} \leq \kappa \leq 100\kappa_{knee}$ representing an over-constrained system, $0.1\kappa_{knee} \leq \kappa \leq 10\kappa_{knee}$ representing a constrained system with values near the knee of the curve, and $0.01\kappa_{knee} \leq \kappa \leq \kappa_{knee}$ representing an under-constrained system. The inset shows the L-curve where the regions corresponding to each solution are marked with thick lines. (b) The measured IPCE and the IPCE curves recalculated with equation (2) using the $\phi(z)$ curves from (a). The IPCE measurement is as in Figure 2(a) and the potential is 1.5 V vs RHE.

Loss mechanisms analysis in material stacks and majority carrier limited materials

The proposed method can offer insights into the charge transfer efficiency across interfaces in material stacks and yields specific terms describing the transport across each of the interfaces. For example, in a water splitting heterojunction photoelectrode, the collection efficiency can be written as $\phi(z) = \phi_i\phi_r\phi_b(z)$. In this case, ϕ_i and ϕ_r are the injection efficiencies of the heterojunction interface and the surface reactivity, respectively. Identification of the specific values of each of these coefficients requires a detailed set of control experiments with small modifications to the structure. For example, testing the same absorber material with and without underlayers can yield information on the contribution of the underlayer to suppressing recombination at the back surface.

It should be noted that the components of the SCE described above should be analyzed based on the specific structures that are being studied. For example, in materials where current is limited by majority charge carriers and the photovoltage is generated near the interface with the electrolyte (such as $BiVO_4$[5,6]) increasing the thickness of the material increases the distance majority carriers need to traverse before being collected, thus increasing the probability they will recombine. Hence, the bulk collection efficiency, $\phi_b(z)$ cannot be assumed to be 1 near any of the interfaces. Assigning specific values to the different injection efficiencies may be done by studying reference material stacks in which properties of some of the interfaces are well known or by applying complementary techniques, such as intensity

modulated photocurrent spectroscopy or transient photocurrent spectroscopy, to complete the picture of more complex systems. In addition, for materials in which geminate recombination is significant or in which optical absorption from on-site *d-d* transitions overlaps with the extended absorption spectrum, a term describing the probability that absorbed photons generate mobile carriers should also be added. In this respect, quantifying geminate recombination using, for example, transient optical spectroscopies and identifying different optical transitions by applying knowledge of electronic structure of the material would aid in quantifying loss mechanisms.

Sources for uncertainties in extracted $\phi(z)$ profiles and collection lengths

We define the regularization spread as the standard deviation between all the averaged solutions. Figure S9 (a) shows the extracted $\phi(z)$ profile for the first 30 nm below the surface, as shown in Figure 2(b) at a potential of 1.5V vs RHE. Profiles were averaged for regularization parameters in the range $0.1\kappa_{knee} \leq \kappa \leq 10\kappa_{knee}$. The gray area marks the regularization spread. The inset is a full view of the $\phi(z)$ profile. Although the regularization spread is very small in most of the sample, it increases significantly in the active regions. Such deviations in the extracted solutions can be a result of measurement errors, optical modeling errors, or because the spectral window used for the IPCE measurement is too narrow. Figure S9(b) shows the front and back illumination IPCE measurements at the same potential. The error bars mark the standard deviation of seven different IPCE measurements. According to equation (2), deviations in the measured current cause deviations with similar proportions in the $\phi(z)$ profile. Thus, since the error bars in the IPCE measurements are much smaller than the regularization spread in Figure S9(a), it can be concluded that the contribution of the measurement errors and noise to the uncertainty is relatively small. Figure S9(c) shows the modeled and measured optical absorptance in the same wavelengths range as Figure S9(b). The oscillating behavior of the modeled curve is a result of interference patterns caused by forward and backwards propagating waves. This behavior is slightly suppressed in the measured curves because of the finite roughness of the sample, which leads to light scattering. Figure S9(d) shows the measured IPCE and the IPCE recalculated with equation (2) using the mean $\phi(z)$ profile from Figure S9 (a). The reconstructed IPCE curves show an oscillatory behavior that deviates from the measured curves in the same wavelength range as the deviation between the modeled and measured optics. This indicates that the optical modeling errors are preventing the regularization process from converging to a single physical solution. Apart for improving the optical modeling, which can be done by adding scattering effects to the models, the regularization spread can be reduced by adding more information about the photoanode behavior near its surface. At a wavelength of 350 nm, the optical absorption depth of the γ-$Cu_3V_2O_8$ layer is about 50 nm. Thus, even at this short wavelength, most of the photons are absorbed away from active region, leading to a fairly low current output. Extending the IPCE measurement to shorter wavelengths, where most of the incident photons are absorbed within the active region can help reduce these uncertainties.

As discussed in the main text, the collection length is defined as the distance at which the SCE reaches 0.1 of its value at the surface, i.e. $\phi(L_c) = 0.1\phi(0)$. The white circle in Figure S9(a) marks this point. The regularization spread also imposes an uncertainty on the extracted collection length. The upper and lower bounds for the collection length are the maximum and minimum distances at which the extracted SCE profiles, including the regularization spread, reach $0.1\phi(0)$, respectively. These bounds are marked by the dashed lines in Figure S9(a) and the difference between the two bounds is the uncertainty in the collection length, ΔL_c, which is marked by the error bars in Figure 4 in the main text.

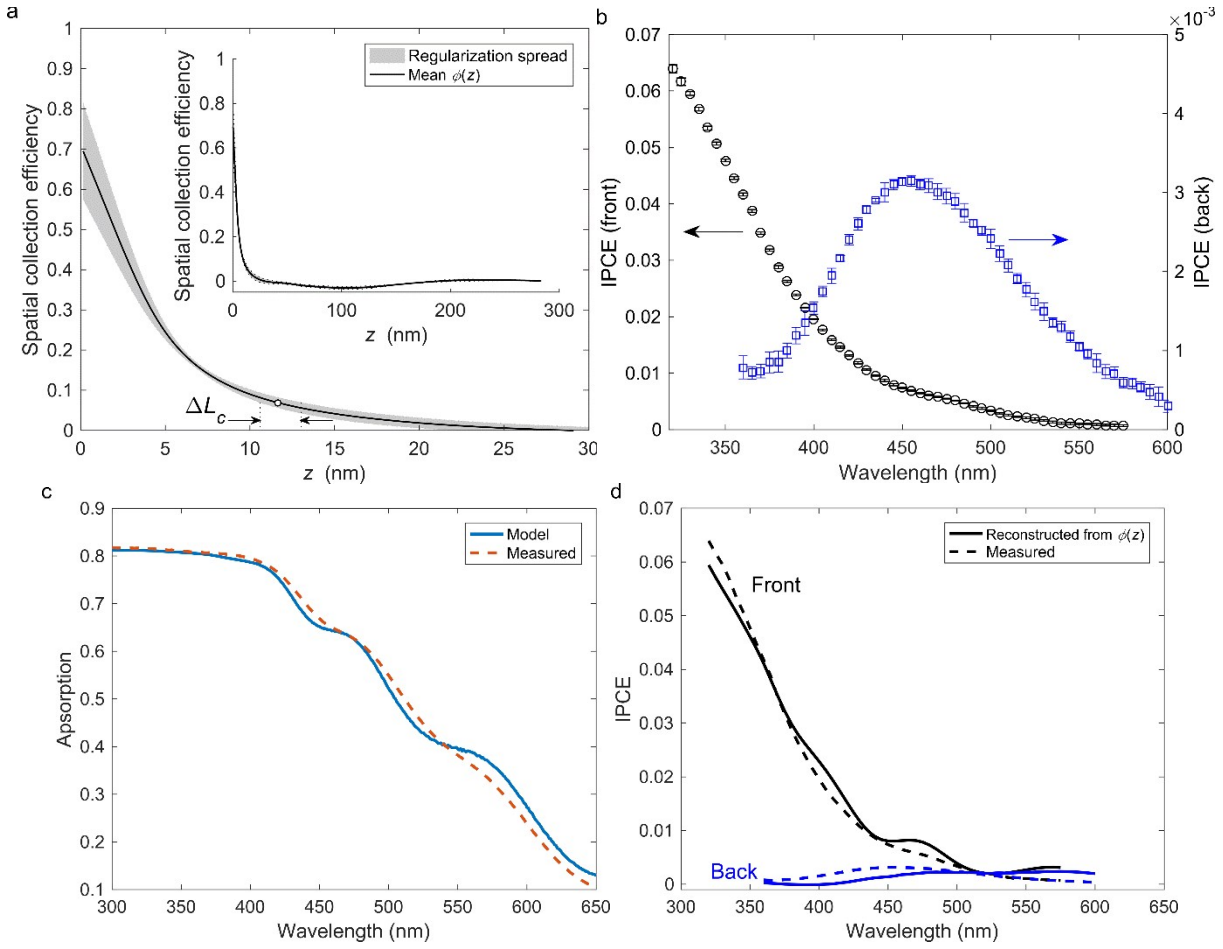

Figure S9: (a) The extracted $\phi(z)$ curves from γ-$Cu_3V_2O_8$ at a potential of 1.5 V vs RHE. Curves were averaged for regularization parameters in the range of $0.1\kappa_{knee} \leq \kappa \leq 10\kappa_{knee}$. The gray area marks the regularization spread, the white circle marks the point used to calculate the collection length and the dashed lines mark the upper and lower bounds for the collection length considering the regularization spread. The uncertainty in the value of the collection length, ΔL_c, is the difference between the two bounds. The inset is a zoom-in of the first 30 nm of the sample. (b) IPCE measured under front and back illumination at a potnetial of 1.5 V vs. RHE. The error bars mark the standard deviation between seven IPCE measurments. (c) The measured and calculated optical absorption of the γ-$Cu_3V_2O_8$ sample. (d) The measured IPCE and the IPCE recalculated with equation (2) using the $\phi(z)$ curve from (a).

Mott-Schottky Analysis

Mott-Schottky analysis was performed in order to estimate the active donor concentration in the bulk of the γ-$Cu_3V_2O_8$ photoanode. Impedance spectroscopy measurements were conducted using a Bio-Logic SP-300 potentiostat in a pH 9.3, 0.1 M sodium borate buffer electrolyte with 0.1 M Na_2SO_3 as a sacrificial hole acceptor. The frequency range measured was between 0.3 Hz and 30 kHz and the potential range was between 0.55 V and 1.35 V vs RHE. Figure S10 shows Nyquist plots produced by the analysis for potentials between 1 V and 1.3 V vs RHE. Figure S11 shows the Mott-Schottky analysis produced by fitting the impedance spectroscopy data to a single RC circuit. Curves between frequencies of 15 Hz and 13 kHz show a linear region, from which an estimation of the flat band potential (intercept with the horizontal axis) and dopant concentration (slope) can be deduced.[7] The curves show a frequency dependence which may be a result of non-uniform dopant concentrations or other inhomogeneities within the sample. Hence only a rough estimation of the flat band potential and dopant concentration can be given. Assuming a permittivity that is similar to Hematite, i.e. close to 20, an active donor concentration of about 10^{19} cm^{-3} is determined for all frequencies analyzed. The flat band potential extracted is between 0.45 V and 0.55 V vs. RHE for all the frequencies measured. This value is slightly lower than the current onset potential shown in the inset of Figure 2(a).

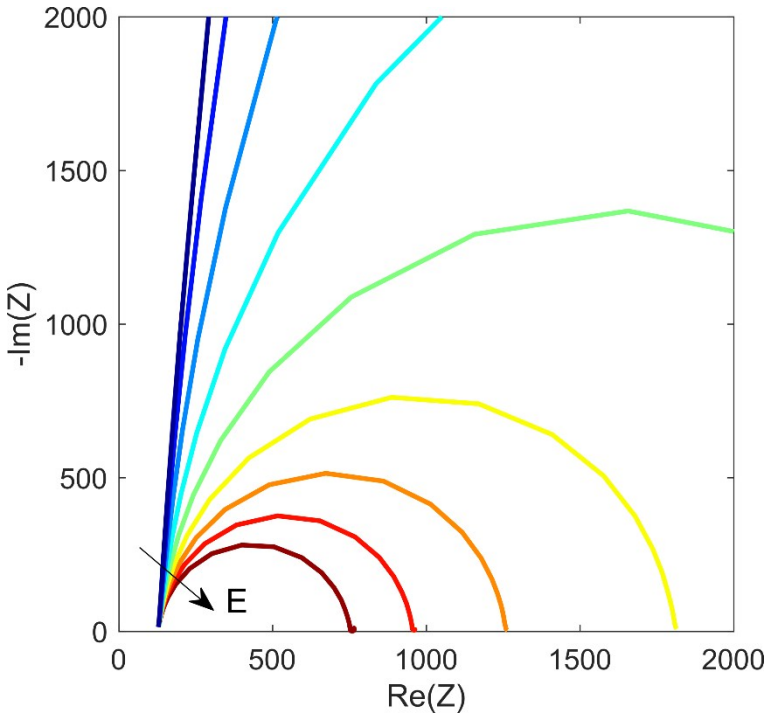

Figure S10: Nyquist plots obtained from electrochemical impedance spectroscopy of a γ-$Cu_3V_2O_8$ photoanode in the presence of a sacrificial reagent. The potential range displayed is between 1 and 1.3 V vs RHE and the frequency range is between 0.3 Hz and 30 kHz.

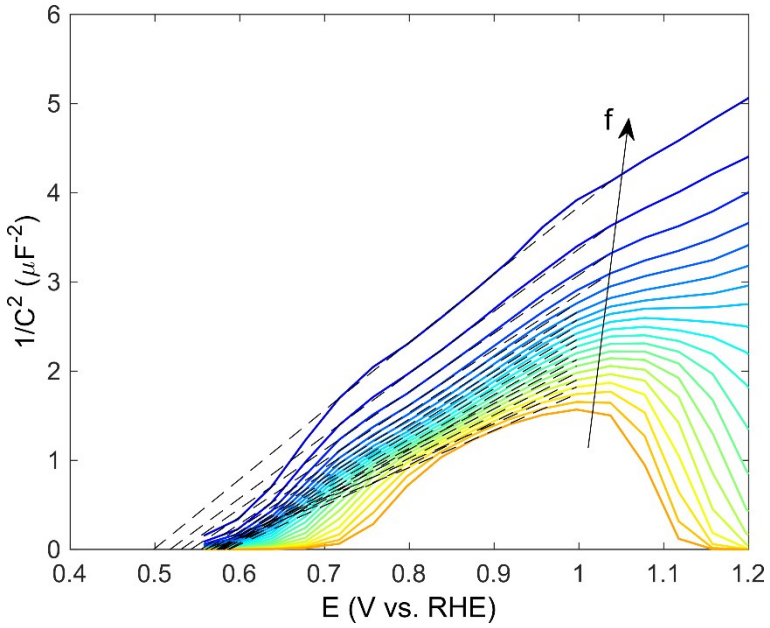

Figure S11: Mott Schottky plots extracted from the electrochemical impedance spectroscopy data in Figure S10 with fits to linear regions of the curves. Curves corresponding to frequencies between 15 Hz and 13 kHz were used to extract estimations for the dopant concentration and flat band potential.

References

1 C.-M. Jiang, M. Farmand, C. H. Wu, Y.-S. Liu, J. Guo, W. S. Drisdell, J. K. Cooper and I. D. Sharp, *Chem. Mater.*, 2017, **29**, 3334–3345.

2 A. N. Tikhonov, A. V. Goncharsky, V. V. Stepanov and A. G. Yagola, *Numerical Methods for the Solution of Ill-Posed*

Problems, 1995.
3 P. C. Hansen, *Numer. Algorithms*, 2007, **46**, 189–194.
4 Y. T. Pang, H. Efstathiadis, D. Dwyer and M. D. Eisaman, *2015 IEEE 42nd Photovolt. Spec. Conf.*, 2015, 15–18.
5 I. D. Sharp, J. K. Cooper, F. M. Toma and R. Buonsanti, *ACS Energy Lett.*, 2017, **2**, 139–150.
6 J. K. Cooper, S. B. Scott, Y. Ling, J. Yang, S. Hao, Y. Li, F. M. Toma, M. Stutzmann, K. V. Lakshmi and I. D. Sharp, *Chem. Mater.*, 2016, **28**, 5761–5771.
7 R. Van De Krol and M. Grätzel, *Photoelectrochemical Hydrogen Production*, 2012, vol. 102.